AGU PUBLICATIONS

Geochemistry, Geophysics, Geosystems

RESEARCH ARTICLE

10.1002/2017GC007281

Key Points:

- Previous seismic studies of ultralow velocity zones are compiled and digitized
- A digital database of the distribution of ultralow velocity zone presence and absence is produced and made publicly available
- Ultralow velocity zones are commonly near low velocity provinces, but many are in presumed cool regions, consistent with being chemically distinct

Correspondence to:
S. Yu,
shule.yu@asu.edu

Citation:
Yu, S., & Garnero, E. J. (2018). Ultra-low velocity zone locations: A global assessment. *Geochemistry, Geophysics, Geosystems*, *19*, 396–414. https://doi.org/10.1002/2017GC007281

Received 10 OCT 2017
Accepted 13 DEC 2017
Accepted article online 19 JAN 2018
Published online 7 FEB 2018

Ultralow Velocity Zone Locations: A Global Assessment

Shule Yu[1] and Edward J. Garnero[1]

[1]School of Earth and Space Exploration, Arizona State University, Tempe, AZ, USA

Abstract We have compiled all previous ultralow velocity zone (ULVZ) studies, and digitized their core-mantle boundary (CMB) sampling locations. For studies that presented sampling locations based on infinite frequency ray theory, we approximated Fresnel zones onto a 0.5° × 0.5° grid. Results for these studies were separated according to wave type: (1) core-reflected phases, which have a single location of ULVZ sampling (ScS, ScP, PcP), (2) core waves that can sample ULVZs at the core entrance and exit locations of the wave (e.g., SP_dKS, PKKP, and PKP), and (3) waves which have uncertainties of ULVZ location due to long CMB sampling paths, e.g., diffracted energy sampling over a broad region (P_{diff}, S_{diff}). For studies that presented specific modeled ULVZ geographical shapes or PKP scatter probability maps, we digitized the regions. We present summary maps of the ULVZ coverage, as well as published locations arguing against ULVZ presence. A key finding is that there is not a simple mapping between lowermost mantle reduced tomographic velocities and observed ULVZ locations, especially given the presence of ULVZs outside of lowermost mantle large low velocity provinces (LLVPs). Significant location uncertainty exists for some of the ULVZ imaging wave types. Nonetheless, this compilation supports a compositionally distinct origin for at least some ULVZs. ULVZs are more likely to be found near LLVP boundaries, however, their relationship to overlying surface locations of hot spots are less obvious. The new digital ULVZ database is freely available for download.

Plain Language Summary Nearly half way to the center of Earth, small and thin regions of extremely anomalous mantle rock sit on top of Earth's fluid core. The speeds of seismic waves are reduced by tens of percent in these tiny zones, and for over 20 years have been interpreted as being partially molten. Here, we summarize all the past studies and show that the geographical distribution of the sluggish patches is consistent with a requirement that they be compositionally distinct from the surrounding mantle. Their composition remains unknown. Dubbed "ultra-low velocity zones", they remain enigmatic - less than 20% of Earth's core mantle boundary has been explored in past investigations. However, this summary suggests they have a preference of being located near the margins of two much larger anomalies, continental-sized lowermost mantle low seismic wave speed provinces.

1. Introduction

1.1. ULVZ Properties and Origin

In the past two decades, seismic investigations of deep mantle heterogeneity have reported thin, patch-like mantle-side seismic anomalies adjacent to the core-mantle boundary (CMB) with strong velocity reductions. The reported ultralow velocity zone (ULVZ) properties vary: thicknesses range from 3 to 100 km, but are most commonly tens of kilometers (e.g., He & Wen, 2009; Rost et al., 2010a; Thorne & Garnero, 2004), *P* wave velocity reductions are up to 25% (e.g., Brown et al., 2015; Ross et al., 2004), *S* wave velocity reductions are up to 50% (e.g., Idehara, 2011; Rondenay & Fischer, 2003), density increases are up to 20% (e.g., Idehara, 2011; Koper & Pyle, 2004), and lateral sizes range from tens of kilometers up to around 900 km (e.g., Cottaar & Romanowicz, 2012; Jensen et al., 2013; Yuan & Romanowicz, 2017). Occasionally, varying properties within ULVZs are proposed. These may include a diffusive top or a vertical velocity gradient (e.g., Rondenay & Fischer, 2003; Rost et al., 2006), or multilayered structures (e.g., Idehara, 2011; Pachhai et al., 2015; Ross et al., 2004). Using 2 + D synthetic seismogram modeling, different ULVZ three-dimensional shapes have been presented, including box-car, dome, and Gaussian shapes (e.g., Cottaar & Romanowicz, 2012; Thorne et al., 2013; To et al., 2011; Wen & Helmberger, 1998b; Yuan & Romanowicz, 2017).

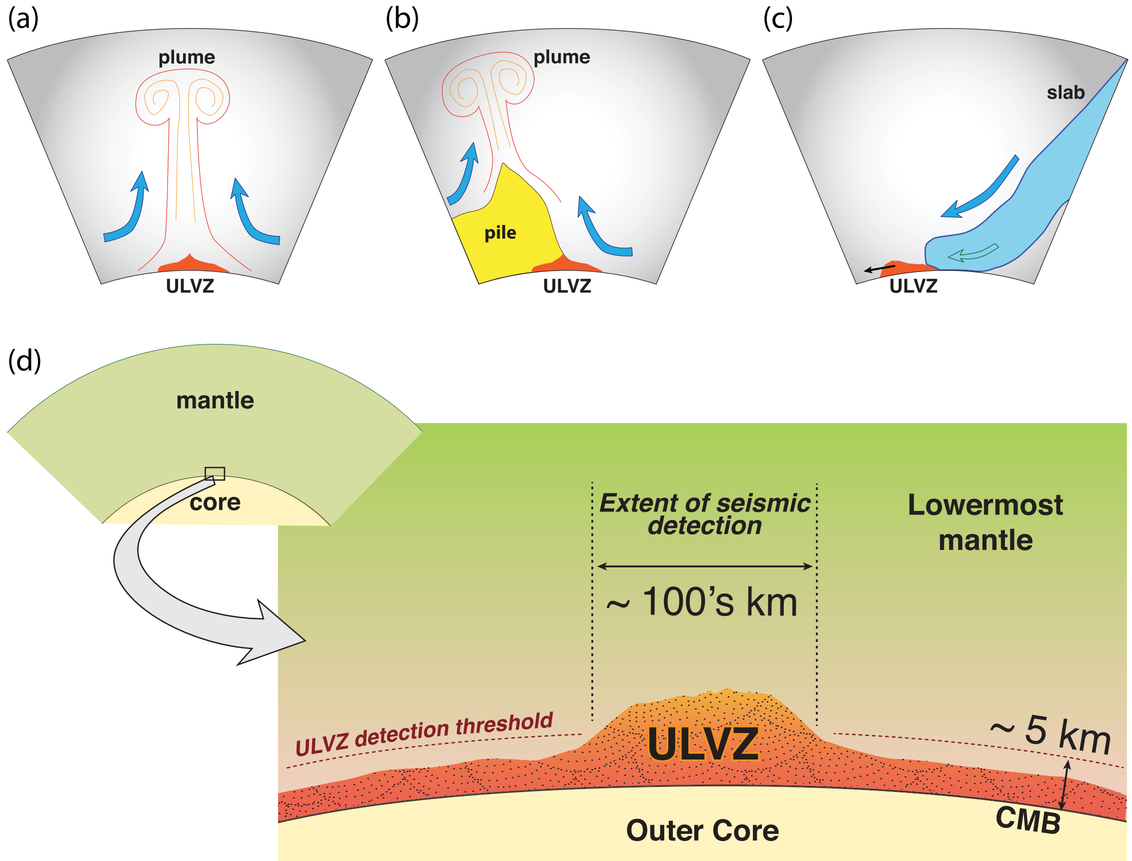

Figure 1. Cartoons showing ULVZ detection locations and other phenomena. (a) ULVZs have been reported to exist beneath surface hot spots, associated with mantle plumes. Arrows indicate large-scale mantle flow. These basal zones may be the hottest deep mantle locations, and relate to the origin of partial melt in ULVZs. (b) Compositionally distinct ULVZs will advect to the margins of thermochemical piles, which have been advocated as the origin of LLVPs. (c) ULVZs in relatively cold regions might be due to deeply subducted oceanic crust, or possible accumulated products of chemical reactions between the core and mantle. Subduction-related flow can advect these ULVZs toward LLVP regions. (d) The possibility of widespread thin ULVZs. They are seismically imaged only when the accumulated thickness of ULVZ material extends off the CMB above the seismic resolution limitations (roughly 5 km vertically, depending on the seismic phase and ULVZ properties). This cartoon depicts a detectable ULVZ with lateral dimension of hundreds of kilometers.

Many possible origins to ULVZs have been proposed, and essentially emphasize the role of very high temperature or chemically altered (and distinct) compositions. The modeled 3:1 ratio in *S* wave to *P* wave velocity reduction can be explained by 5–30% partial melting of the deepest mantle material (Berryman, 2000; Williams & Garnero, 1996), with the amount of melt depending on actual melt geometry (e.g., Williams & Garnero, 1996). Seismic wavefield scattering studies have also suggested a possible melt origin to small scale heterogeneities (Thomas et al., 2009). ULVZs located beneath the surface locations of hot spots (e.g., Cottaar & Romanowicz, 2012; Rost et al., 2005; Yuan & Romanowicz, 2017) may point to a thermal origin (Figure 1a), though this does not preclude compositionally distinct material having been advected to plume root locations. The partial melt explanation faces difficulties in explaining ULVZs detected around the edge, or away from presumably hotter lowermost mantle regions (i.e., the large low velocity provinces, LLVPs) (Luo et al., 2001; Ni & Helmberger, 2001b; Rondenay & Fischer, 2003; Ross et al., 2004; Xu & Koper, 2009). Also, we may expect to see more ULVZs in the center of LLVPs if their origin is related to the hottest mantle temperatures. Thermodynamical arguments advocate the necessity of compositional distinction to ULVZs (Hernlund & Tackley, 2007). Nonetheless, their existence around the edge of LLVPs (Figure 1b) combined with a proposed density elevation (Havens & Revenaugh, 2001; Ross et al., 2004; Thorne & Garnero, 2004) appears compatible with a compositional difference between ULVZs and the surrounding mantle (Li et al., 2017; McNamara et al., 2010). Various hypotheses have invoked iron-enrichment to account for the observed ULVZ density elevation (Dobson & Brodholt, 2005; Mao et al., 2006; Tsuchiya & Tsuchiya, 2006; Wicks et al., 2017). The subduction of basaltic oceanic crust could bring chemically distinct materials to the lower mantle, which may explain the sporadic ULVZ distribution as well as compositional uniqueness (Andrault et al., 2014; Hu et al., 2016; Liu et al., 2016; Nomura et al., 2014). Other possibilities exist, e.g., products from chemical reactions between the silicate mantle and core (Buffett et al., 2000), which could give rise to ULVZs far from LLVPs. These possibilities (and others) would result in ULVZ material which will then be swept toward upwelling regions (Figure 1c). It is noteworthy to mention that resolution issues may be at play that result in ULVZs erroneously going undetected (Figure 1d). That is, ULVZs may be missed if they are especially thin, e.g., $<$3–5 km (Ross et al., 2004; Rost & Thomas, 2010), or if they have three-dimensional structure that masks their detection. However, thin ULVZ possessing particularly anomalous properties have a better chance at being detected, especially with waves that depend upon velocities right at the CMB, like SP_dKS. The focus of this work is a comprehensive assessment of ULVZ distribution and properties, which is warranted before advocating any particular origin to ULVZs.

1.2. ULVZ Seismic Probes

A summary of seismic phases used in previous ULVZ studies is presented in Figure 2. These phases share a common feature in that they interact with the CMB, and thus hold opportunity to detect and image ULVZ structure. In this study, we group results from previous investigations according to the type of seismic wave: namely, (1) a CMB reflection, (2) a core wave with different core entry and exit locations, (3) CMB diffraction, and (4) scattering at the CMB. A reflected wave (including ScS, ScP, and PcP) samples the CMB once, at the reflection point (Figure 2a). If the ULVZ has an abrupt discontinuity at the top (and is locally flat to first order), a reflection off the top of the ULVZ will result in a precursory (early) arrival relative to the main phase. Internal reflections or P-to-S or S-to-P conversions within the ULVZ layer can result in additional delayed arrivals (post-cursors) relative to the main phase (Figures 2b–2d). Therefore analyses of CMB reflected waves for investigating ULVZ structure commonly utilize the timings and amplitudes of precursors and postcursors (e.g., Avants et al., 2006; Hutko et al., 2009; Rost et al., 2005). Diffracted phases encounter the CMB either once (e.g., P_{diff} and S_{diff}) or twice (e.g., SP_dKS and $PKKP_{ab\_diff}$, Figures 2e and 2h). Reduced seismic wave speeds at the very base of the mantle can cause delays and waveform distortions of the diffracted arrivals. However, since the diffraction paths can be relatively long (e.g., P_{diff} and S_{diff}), or occur at two separate CMB crossing locations (e.g., SP_dKS and $PKKP_{ab\_diff}$), there is uncertainty in uniquely identifying the exact ULVZ location. To resolve the ambiguities of a source-side versus receiver-side location for ULVZ structure (or both), either knowledge from crossing path sampling (e.g., Rondenay & Fischer, 2003) or incorporation of previously published models (e.g., Thorne et al., 2013) is typically required. Detailed waveform modeling utilizing 2-D and 3-D models helps in the imaging, but introducing a larger model space can introduce more trade-offs (e.g., Cottaar & Romanowicz, 2012; Thorne et al., 2013; To et al., 2011). PKP used in waveform studies also encounter the CMB twice, and thus can involve source-side versus receiver-side ULVZ location ambiguity (e.g., Thomas et al., 2009; Wen & Helmberger, 1998a). In contrast, scattered PKP observed at precritical distance and identified by azimuth-slowness analyses (Figures 2j and 2k) circumvent the source-receiver-side uncertainty by pointing to specific scattering heterogeneities.

1.3. ULVZ Distribution

The study of McNamara et al. (2010) summarized over 40 ULVZ studies and produced a ULVZ distribution map, suggesting that ULVZs are preferably grouped around LLVP regions. However, as they also noted, many ULVZs were not within or near LLVPs. The ULVZ regions presented in that study were graphically redrawn from previous studies; that is, they were not digitally reproduced. In this study, we digitize these regions (including ULVZ regions from more recent studies). This enables a more quantitative comparison of ULVZ locations to other lower mantle related phenomena, such as LLVPs and hot spots. In addition to geographical comparisons, the database presented here is publically available (Yu & Garnero, 2017).

2. Digitizing ULVZ Regions

2.1. ULVZ Information Collection

We have surveyed all seismologically determined ULVZ regions from studies self-identifying their observations as ULVZs. We applied no filter regarding ULVZ properties such as the degree of velocity drop or ULVZ height. Some ULVZ models do not have a particularly "ultra" velocity drop, but the velocity anomaly exceeds typical maximum levels in lowermost mantle tomography models. This, combined with evidence in many cases for an abrupt change to the reduced velocities, suggests the structure is consistent with the

10.1002/2017GC007281

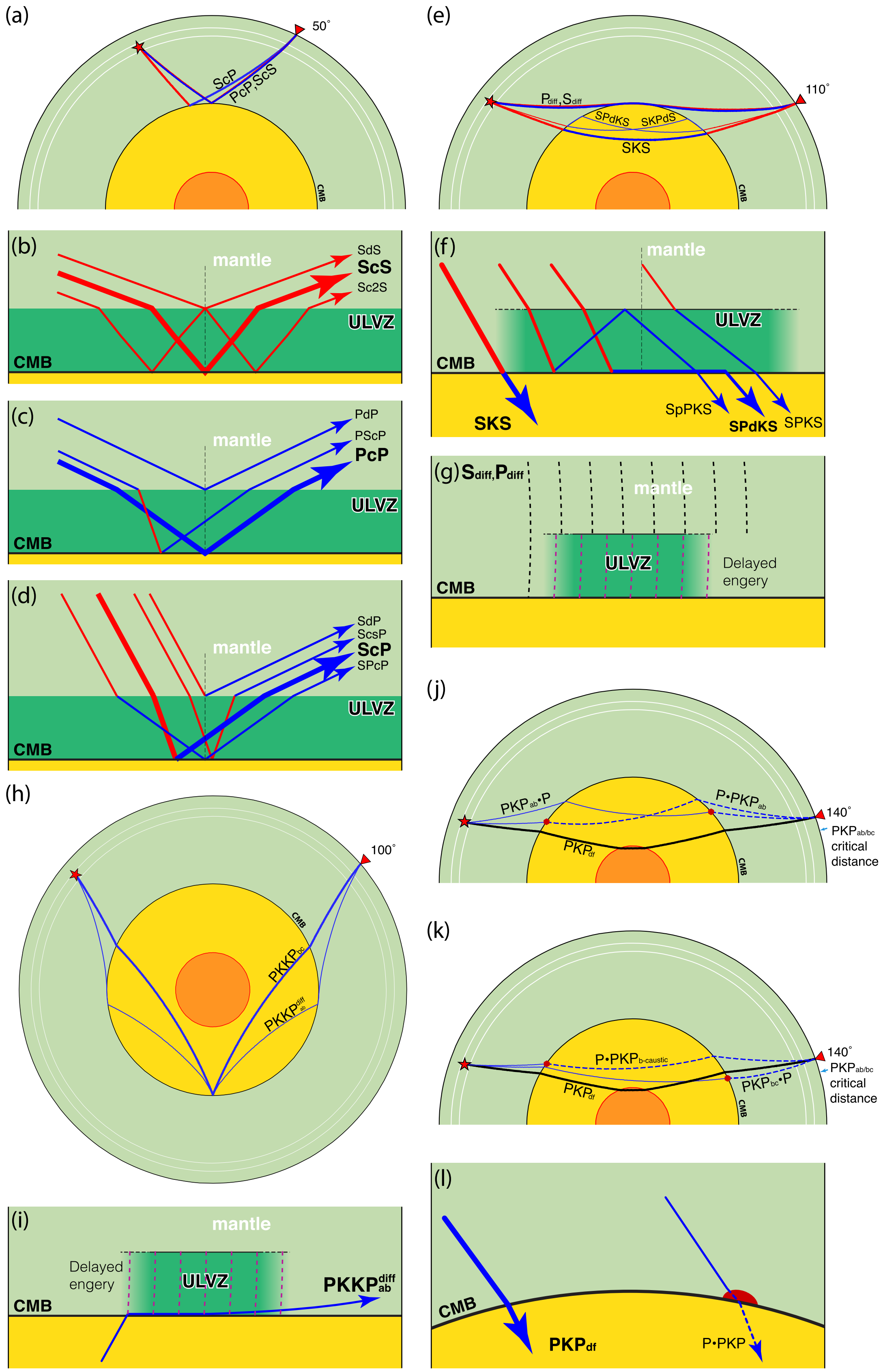

Figure 2. (continued)

ULVZ concept. However, we do not set a filter since our database of past studies separately lists every study. Thus, future work using the database can define ULVZs based on any criteria. A list of previous studies is presented in Table 1. Studies are grouped according to the type of seismic probe, then further grouped by sampling region (the region names in Table 1 are presented in Figure 3). Authors of all studies were emailed with requests for digital ULVZ locations. For studies in which we did not receive digital locations, we proceeded with digitizing ULVZs from figures and tables in their papers. Our database includes three types of raw information for ULVZ locations: (1) CMB reflection point locations for reflected waves, (2) CMB ray path lines where diffraction occurs at the CMB for waves with diffraction, and (3) CMB areas, namely, for (a) PKP wave scattering probability maps, and also for (b) past studies that presented specific ULVZ geographical shapes. Each information entry is either a positive detection with ULVZ properties, a nondetection, or an uncertain detection. The uncertain detections are for complex waveforms which could not be unambiguously modeled, and were described as uncertain in original studies. In our online database, each CMB sampling zone is a single file described by an individual entry in the online database table.

2.2. Digitizing ULVZs

We used the freeware software package GraphClick for Cartesian and Mercator map projections. For other map projections, we utilized the Generic Mapping Tools (GMT) freeware plotting software package (Wessel et al., 2013) and reproduced the map projection in published figures by trial and error (using coastlines and political boundaries for guidance). Once the geographic projection was identified, we digitized ULVZ geographic information from the published figures. For studies of core-reflected waves, the CMB sampling point locations were digitized (these came from 23 studies, corresponding to the following study numbers in Table 1: 2, 4, 9, 12, 13, 15, 16, 18, 22, 24, 27, 28, 29, 30, 33, 34, 37, 38, 40, 41, 42, 50, and 51). If the study binned the sampling points together, the centers of these bins were digitized (this corresponded to three studies: numbers 3, 43, and 53 in Table 1). For studies involving diffraction along the CMB, the end points of each diffraction path were digitized (from four studies: numbers 19, 23, 25, and 31 in Table 1). The ray theoretical diffraction path can be reconstructed by the end points. For studies that reported a specific preferred ULVZ model region, the boundary of the ULVZ region was digitized as a series of points (this came from five studies: numbers 45, 46, 47, 52, and 54 in Table 1). The same process was assumed for studies presenting general ULVZ detection areas, which includes two subcategories: computed Fresnel zone ULVZ areas (four studies: numbers 1, 21, 26, and 49 in Table 1), and PKP scattering high probability regions (four studies: numbers 10, 14, 20, and 48 in Table 1). Additionally, three PKP studies (numbers 6, 32, and 36 in Table 1) and one SKKS study (number 39 in Table 1) designated approximate regions. We note that other studies compared SKKS to SKS for low velocity inference, but did not advocate any particular region for the ULVZ (Zhang et al., 2009) (though this may overlap with other ULVZ study regions) or the structure was not a ULVZ (Silver & Bina, 1993). If a study reported a 2-D cross-section model, we placed the cross section at its geographical position along the great circle path of the reported data, and digitized the two ULVZ edge locations along the cross section (this was done for seven studies: numbers 5, 7, 8, 11, 17, 35, and 44 in Table 1). Regions from study numbers 35 and 44 are further extended azimuthally from the great circle plane to accommodate areas sampled by data (S_{diff} and P_{diff}) presented in those studies. This digital collection of ULVZ locations constitutes what we refer to as the "raw" ULVZ distribution information.

2.3. Approximating Fresnel Zones

As noted, many studies presented CMB sampling location information using infinite frequency ray paths (e.g., reflection points and diffraction lines). Here we use the raw ray path information to approximate

Figure 2. Ray paths of seismic phases used in past ULVZ studies. Sources (red stars) are at 500 km. Receivers are red reversed triangles. Red ray paths represent *S* waves, blue ray paths are *P* waves. Bold ray paths represent reference phases. Gradient ULVZ color represents the uncertainties of its lateral size or top-side shape. (a) ScS, ScP, PcP at 50°. ScS and PcP are nearly identical. Multiple reflections and conversions arise due to a ULVZ layer, and are shown for a flat top ULVZ for ScS in Figure 2b, PcP in Figure 2c, and ScP in Figure 2d. (e) SKS, SP_dKS, SKP_dS and S_{diff}, P_{diff} are shown at 110°. (f) A zoom in the source-side of SKS and SP_dKS in the present of ULVZ. (g) Horizontally propagating S_{diff} and P_{diff} interact with the ULVZ at the CMB. Dashed lines represent diffracted wave fronts which can be delayed enough to affect the overall waveform. (h) $PKKP_{bc}$ and $PKKP_{ab\_diff}$ at 260°. (i) A zoom in at the receiver-side of $PKKP_{ab\_diff}$ depicting its interaction with a ULVZ. (j and k) Examples of scattered PKP ray paths received before the PKP-caustic critical distance are depicted. (l) A zoomed in look at source-side of PKP_{df} showing scattered P energy.

Table 1
A Summary of all Past ULVZ Studies Surveyed Here, Grouped According to Seismic Wave Used to Probe ULVZ Structure

No.	Reference	Phase and method[a]	Region and detection[b]
54	Yuan and Romanowicz (2017)	S_{diff} (t,w)	Iceland (y)
45	Cottaar and Romanowicz (2012)	S_{diff} (a,t,w)	Central Pacific (y)
44	To et al. (2011)	S_{diff} (t,w)	Central Pacific (y,c)
35	Xu and Koper (2009)	P_{diff} (a,t)	Northwest Pacific (y)
31	Rost and Garnero (2006)	$PKKP_{ab\_diff}$ (a,t)	North Atlantic (y)
46	Thorne et al. (2013)	SKS (w)	Southwest Pacific (y)
7	Wen and Helmberger (1998b)	SKS (w)	Southwest Pacific (y)
47	Jensen et al. (2013)	SKS (w)	Coral Sea (y), Philippine Sea (n), South China Sea (y), Celebes Sea (y)
25	Thorne and Garnero (2004)	SKS (w)	Global (y,n,c)
23	Rondenay and Fischer (2003)	SKS (w)	North America (y,n), Northwest Pacific (n)
19	Ni and Helmberger (2001b)	SKS (w)	Central Africa (y,n)
11	Helmberger et al. (2000)	SKS (w)	Central Africa (y), North Atlantic (y)
5	Helmberger et al. (1998)	SKS (w)	Iceland (y)
52	Vanacore et al. (2016)	SKS (w)	South Atlantic (y), West Pacific (c), South America (c)
36	Thomas et al. (2009)	PKP (a,w)	Coral Sea (y), West Pacific (c), Tasman Sea (n)
32	Zou et al. (2007)	PKP (a,s)	Amazon (y)
48	Yao and Wen (2014)	PKP (t,s)	South China Sea (y), Celebes Sea (y)
20	Niu and Wen (2001)	PKP (s)	Central America (y)
14	Wen (2000)	PKP (s)	North Madagascar (y)
17	Luo et al. (2001)	PKP (t,w)	Central Pacific (y,n,c)
10	Thomas et al. (1999)	PKP (s)	Southwest Pacific (y), Europe (y)
6	Vidale and Hedlin (1998)	PKP (s)	Southwest Pacific (y)
8	Wen and Helmberger (1998a)	PKP (w)	Southwest Pacific (y)
39	Sun et al. (2009)	SKKS (t)	South Africa (c)
26	Ross et al. (2004)	PcP (w)	North Siberia (y), West Siberia (n,c)
41	Rost et al. (2010b)	PcP (w)	Northeast Pacific (n)
40	Rost and Thomas (2010)	PcP (m)	Alaska (n)
1	Vidale and Benz (1992)	ScP (w)	Alaska (n)
3	Revenaugh and Meyer (1997)	PcP (t,m)	Alaska (y), Central America (c), Central Pacific (y)
37	Hutko et al. (2009)	PcP (w)	Alaska (c), Central America (n), Central Pacific (y)
21	Persh et al. (2001)	SdP/ScP (r), PdP/PcP (r)	Alaska (n), Central America (n)
12	Castle and Van Der Hilst (2000)	ScP/P (r)	Alaska (n), Central America (n)
4	Kohler et al. (1997)	PcP (w)	Alaska (n), Central Pacific (y)
16	Havens and Revenaugh (2001)	PcP (m)	Central America (y,n,c)
29	Avants et al. (2006)	ScS (m)	Central America (n), Central Pacific (y)
2	Mori and Helmberger (1995)	PcP (w)	Central America (n), Central Pacific (y)
33	Courtier et al. (2007)	ScS (m)	Central Pacific (c)
53	Zhao et al. (2017)	ScS (w)	Central Pacific (y)
49	Gassner et al. (2015)	PcP (w)	Europe (y,n)
43	Idehara (2011)	ScP (w)	Philippine Sea (y,n,c)
34	Idehara et al. (2007)	ScP (w)	Celebes Sea (y,n), Philippine Sea (y,n), Coral Sea (y,n), Banda Sea (n)
50	Pachhai et al. (2015)	ScP (w)	Philippine Sea (y), Tasman Sea (y)
28	Rost et al. (2005)	ScP (w)	Coral Sea (y,n,c)
30	Rost et al. (2006)	ScP (w)	Coral Sea (y,n,c)
42	Rost et al. (2010a)	ScP (w)	Coral Sea (y,n)
51	Brown et al. (2015)	ScP (w)	Coral Sea (y)
24	Rost and Revenaugh (2003)	ScP (w)	Coral Sea (y,n)
15	Rost and Revenaugh (2001)	ScP (w)	Coral Sea (y)
27	Koper and Pyle (2004)	PKiKP/PcP (r)	Coral Sea (y)
38	He and Wen (2009)	ScS (t,w)	West Pacific (y)
13	Reasoner and Revenaugh (2000)	ScP (w)	Southwest Pacific (y,n,c), West Pacific (c)
9	Garnero and Vidale (1999)	ScP (w)	Southwest Pacific (y,n,c), West Pacific (n)
18	Ni and Helmberger (2001a)	ScS (t,w)	South Atlantic (y,c)
22	Simmons and Grand (2002)	ScS, PcP (t)	South Atlantic (y)

[a]Methods used: (a)rray-analysis, 1-D (m)igration, (s)catters, (t)ravel-time, (w)aveform modeling, amplitude (r)atio. [b]Detection classification: (y)es detection, (n)o detection, (c)omplex or uncertain observations.

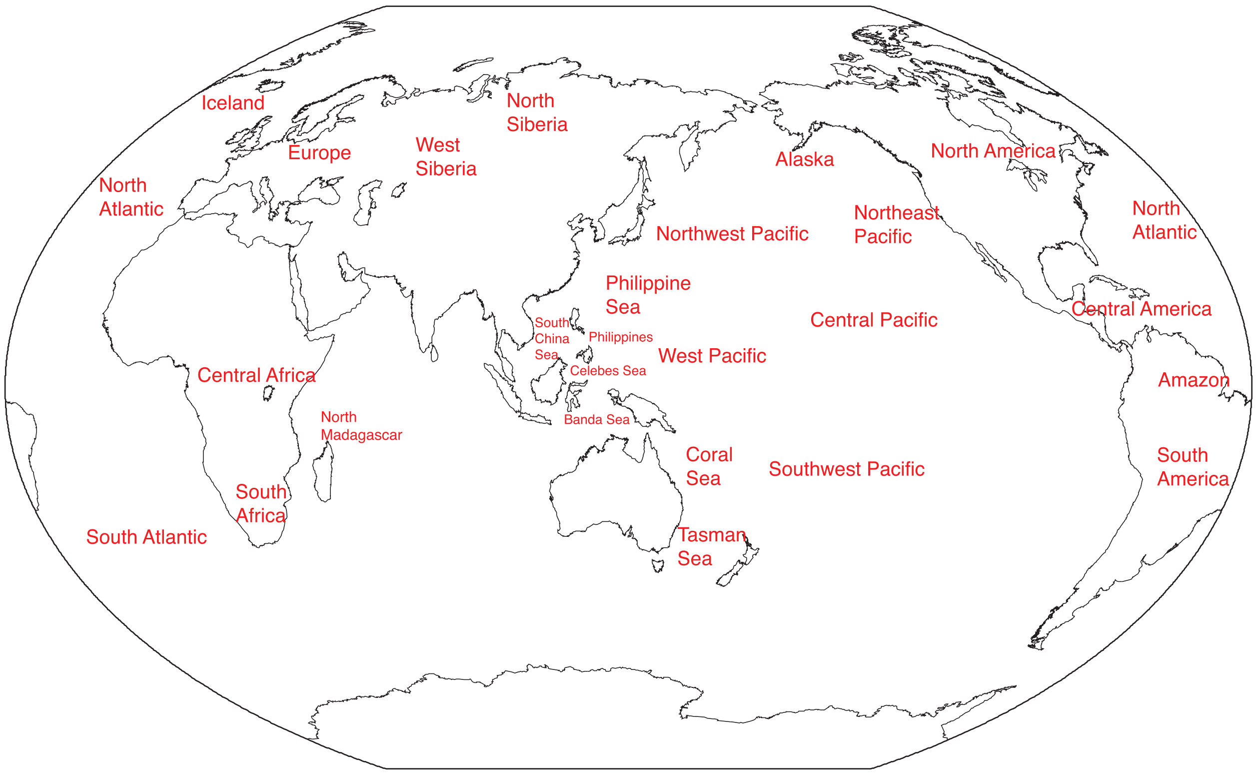

Figure 3. Map showing location region naming convention used in Table 1.

Fresnel zones, in order to more realistically consider the spatial distribution of ULVZs. For CMB reflected phases, we conduct a grid search on the CMB around the ray theoretical bounce point location to find all grid points rendering source-to-CMB-to-receiver travel times within a quarter of the dominant period (Figure 4a). The dominant periods were either discerned from data shown in the original papers, or assumed, using the published corner frequencies in filters used on the seismic data. The path geometry (i.e., great circle distance and azimuths for different studies) was either calculated from event-station location information or measured on maps (see online database table for the values of dominant periods, azimuths, and distances of each study). In practice, we found the resulting Fresnel zones could be well approximated by ellipses. Thus, using the period and path geometry information, we found the elliptical estimate of the Fresnel zone for each reflected wave. For diffracted wave studies, we similarly constructed ellipses to

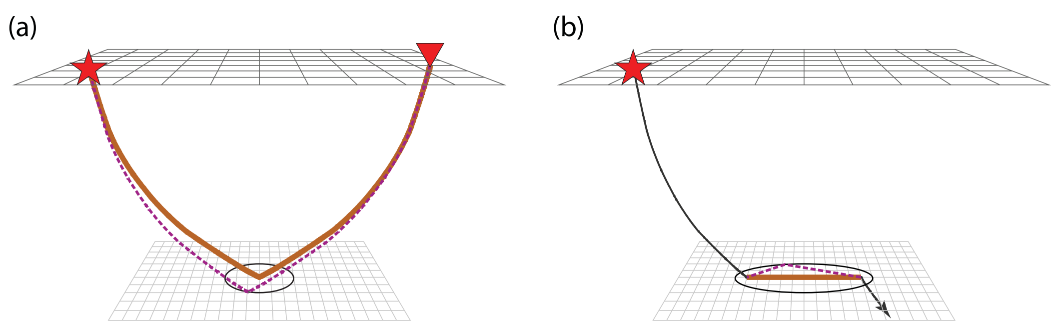

Figure 4. Schematic plot depicting addition of Fresnel zone approximations. Stars represent events and reversed triangle represents the seismic station at Earth's surface. The lower grid represents the CMB. (a) Fresnel zone approximation ellipse around sampling points of PcP, ScP, and ScS. An ellipse on the CMB is found such that for each point on it, the travel time difference between original ray path (brown) and an alternative ray path (dashed purple) is equal to one quarter dominant period of the data. (b) Fresnel zone approximation ellipse around a CMB diffraction segment; this segment could be the P-diffraction part of SP_dKS (shown), as well as SKP_dS and $PKKP_{ab\_diff}$.

approximate Fresnel zones for the diffracted segment of the wave path (again, assuming quarter wavelength for the time of the diffraction sampling the elliptical zone, Figure 4b). This technique was also applied to studies whose raw information involved ULVZ edge locations from published 2-D cross-section models. We emphasize this method is approximate, but adequate given (a) the diverse and sometimes incomplete nature of the information provided from the past studies; (b) the CMB is not well sampled by ULVZ probing studies due to limitations in source-receiver geometries, thus the conclusions based on our derived sampling zones will not be compromised; (c) ULVZ structure can vary over sub-Fresnel zone scales, thus overemphasizing a computed Fresnel zone for any one study may not be warranted; (d) a majority of past ULVZ studies employed 1-D modeling approaches, thus ULVZ locations and shapes may be offset from solution models (and thus, that which is estimated here), e.g., see (Brown et al., 2015) supplementary information; and (e) a ULVZ nondetection does not preclude ULVZ presence with a thickness smaller than 5 km or so. These interesting but complicating factors are discussed further later in this paper.

3. Results

We present the raw digitized ULVZ distribution information in Figure 5a (Figure 5b presents the same map with numbers corresponding to studies in Table 1). Both detections and nondetections are shown. The sampling area size differs among studies: ULVZs mapped with diffracted waves, including S_{diff}, P_{diff}, and SP_dKS, account for a large portion of the sampled area, while studies based on reflected waves amount to much smaller areas. Some regions are characterized as both having and lacking a ULVZ. These disagreements may be due to the ULVZ location detection ambiguity mentioned in section 1.2. Alternatively, fine-scale variations in ULVZ structure may be at play, since different probes are sensitive to structure at different lateral scales (thus may be visible to one probe, but not another).

Most studies have their sampling locations in and around the Pacific Ocean, due to the dominance of source-receiver geometries sampling there. Large low shear velocity provinces (LLSVPs) are shaded pink, and appear to be near most of the positive detections. However, the pattern has some complexities. For example, many ULVZs are detected outside of LLSVPs, suggesting an origin that is independent from LLSVPs for those zones. Also, many non-ULVZ zones are within LLSVPs.

Figure 6 displays the Fresnel zone approximated ULVZ locations, along with mapped ULVZ model locations, resulting in a larger CMB sampling (compare to Figure 5a). The ULVZs outside of LLSVPs are more apparent (Figure 6a), which has a strong contribution from the globally distributed SP_dKS diffraction paths. While many nondetections occur within LLSVPs, a majority of them occur outside of LLSVPs (Figure 6b). Data that are deemed complex (which thus yield uncertainties in ULVZ presence) are presented in Figure 6c, but not interpreted here. The total percentage of CMB area sampled by past ULVZ studies as presented in Figure 6 is 17.1%.

The level of detail about the ULVZ model properties presented in past studies is variable. Some studies present only the *P* wave velocity reduction (δV_P), others, only the *S* wave reduction (δV_S). Some present both, and some additionally report a density increase. Most (but not all) studies provide an estimate of ULVZ thickness. Trade-offs between these parameters have been explored in many studies (e.g., Garnero & Helmberger, 1998; Idehara et al., 2007; Rost et al., 2005; Thorne et al., 2013; Vidale & Hedlin, 1998). We summarize published ULVZ model properties in Figure 7. Plotted properties include *S* wave and *P* wave velocity reduction, density elevation, and ULVZ thickness. While many studies present a range of models that could fit their data reasonably well, only the properties of stated best fitting models are included in this summary figure. A large number of studies advocate a density increase. ULVZ model thicknesses are up to more than 50 km, and as thin as 2.5 km. A majority of the studies that present both *P* and *S* wave reductions conclude the S velocity drop is 2–3 times (or more) of the P velocity drop, plotting with a δV_S:δV_P ratio of 3:1 or 2:1. We note that in many studies, δV_S:δV_P values are a priori fixed at integer levels and not necessarily well constrained.

4. Comparison with Other Phenomena

4.1. ULVZ Relationship With Lowermost Mantle *S* Wave Heterogeneity

Here we explore the possibility of a spatial relationship between ULVZs and larger scale deep mantle heterogeneity, by measuring distances between ULVZs and lowermost mantle *S* wave velocity contours in δV_S

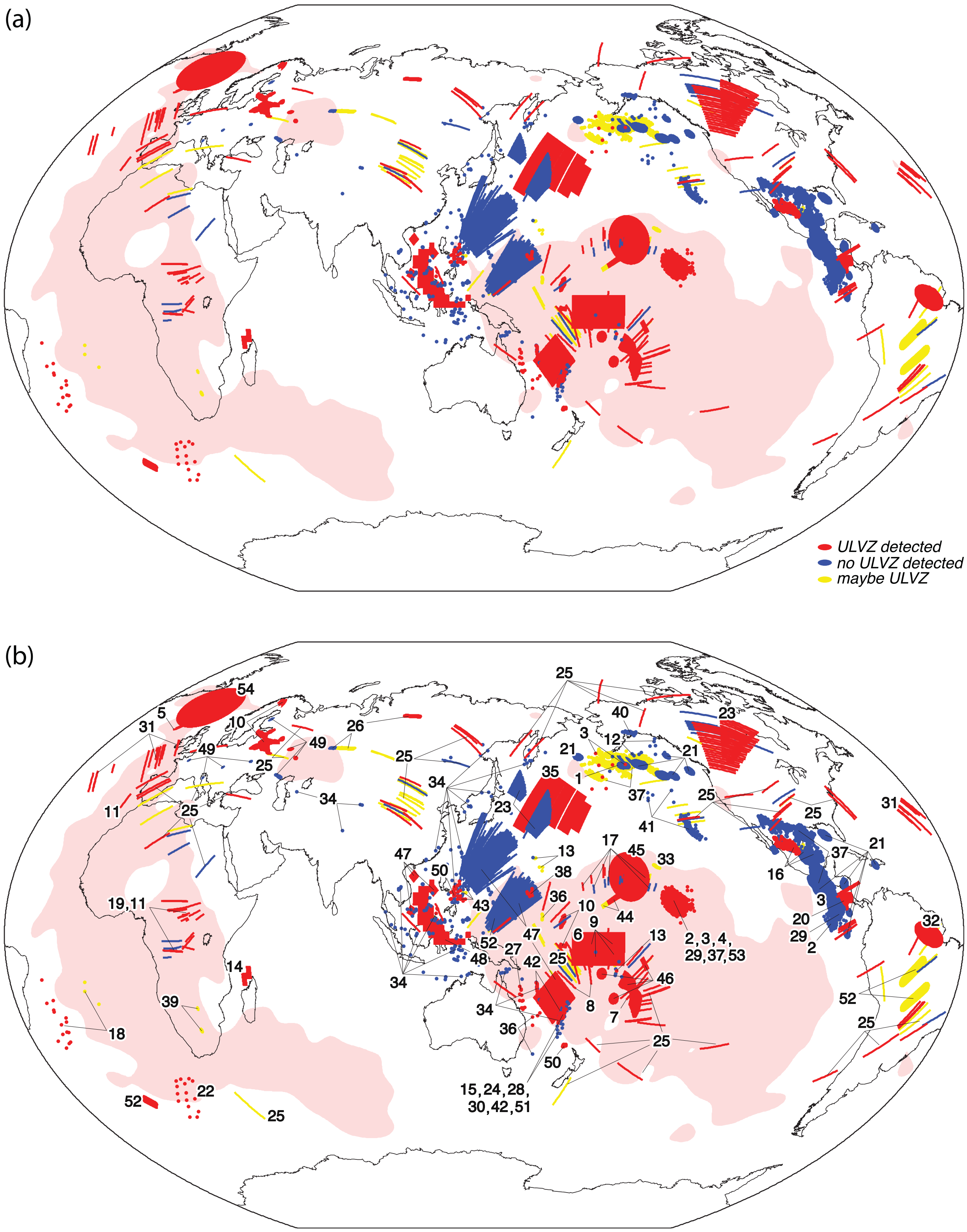

Figure 5. (a) Summary map of ULVZ distribution information from the 54 digitized ULVZ studies in Table 1. Three kinds of ULVZ geographic information are shown here: small circles represent core-reflection locations; lines correspond to CMB diffraction locations as well as regions of 2-D cross-section ULVZ models; and filled areas represent ULVZ models presented in some studies. Colors indicate the presence (red) or absence (blue) of ULVZs; yellow corresponds to complex or uncertain observations. The larger pink regions in the background denote large low shear wave provinces (LLSVPs) from model S40RTS (Ritsema et al., 2011) at depth of 2,800 km. These LLSVPs occupy 30% of the CMB surface area; this corresponds to regions with $\delta V_S \leq -0.27\%$. For plotting clarity, smaller sampling areas are plotted on top of larger ULVZ zones. (b) As in Figure 5a, with the addition of study numbers for each CMB sampling zone, which correspond to first column of Table 1.

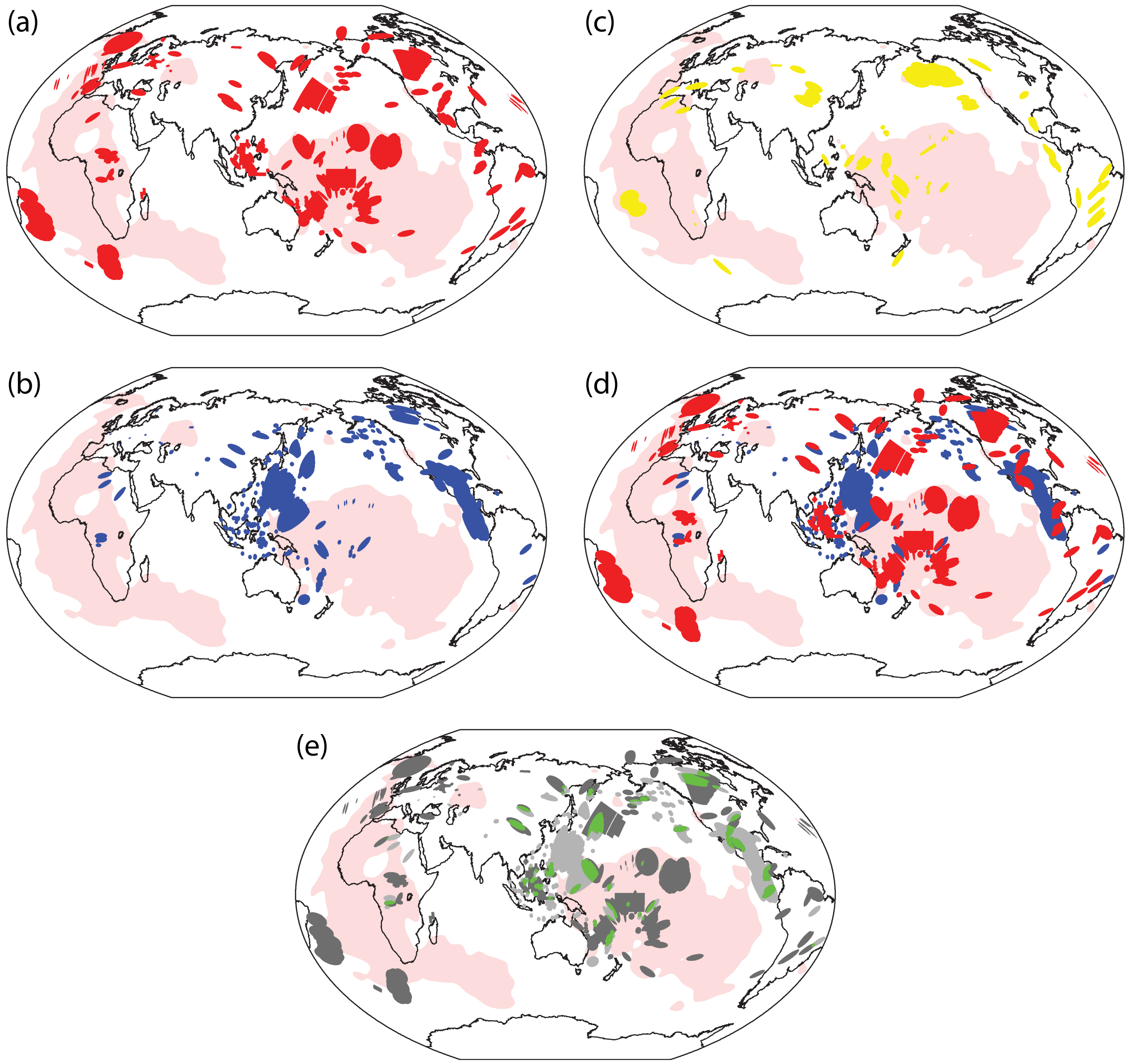

Figure 6. ULVZ distribution information (color scheme as in Figure 5), with the ULVZ point and line information converted to Fresnel zones, for (a) regions with detected ULVZs, (b) regions where ULVZs were not detected, (c) regions with complex waveforms, and (d) the combined information from plots (a) and (b) showing regions possessing and lacking evidence for ULVZs. (e) shows the same regions as in Figure 6d, but the ULVZ and non-ULVZ zones are dark and light gray, respectively, with green regions representing areas showing evidence for both a ULVZ (from plot (a)) and lacking ULVZ (from plot (b)). The pink regions are the LLSVPs as in Figure 5.

tomography models. This is motivated in part because geodynamic studies argue ULVZ material, if chemically dense, will be swept toward thermochemical pile margins (e.g., Hernlund & McNamara, 2015; Li et al., 2017; McNamara et al., 2010), and thermochemical piles are an interpretation for LLVPs (e.g., Garnero et al., 2016; McNamara & Zhong, 2005; Torsvik et al., 2014). On the other hand, if ULVZs are solely due to partial melt of some major lower mantle component (though, argued unlikely, Hernlund & Tackley, 2007), then they would be expected in the hottest regions of the deep mantle, which should be within LLVPs (Li et al., 2017).

We approximate the boundaries of LLSVPs as in Garnero et al. (2016), by choosing a δV_S contour value which encloses 30% of the area of the CMB that contains the lowest velocities in the model. A similar thing is done for the highest δV_S values, which can be speculated to correspond to the coldest lower mantle

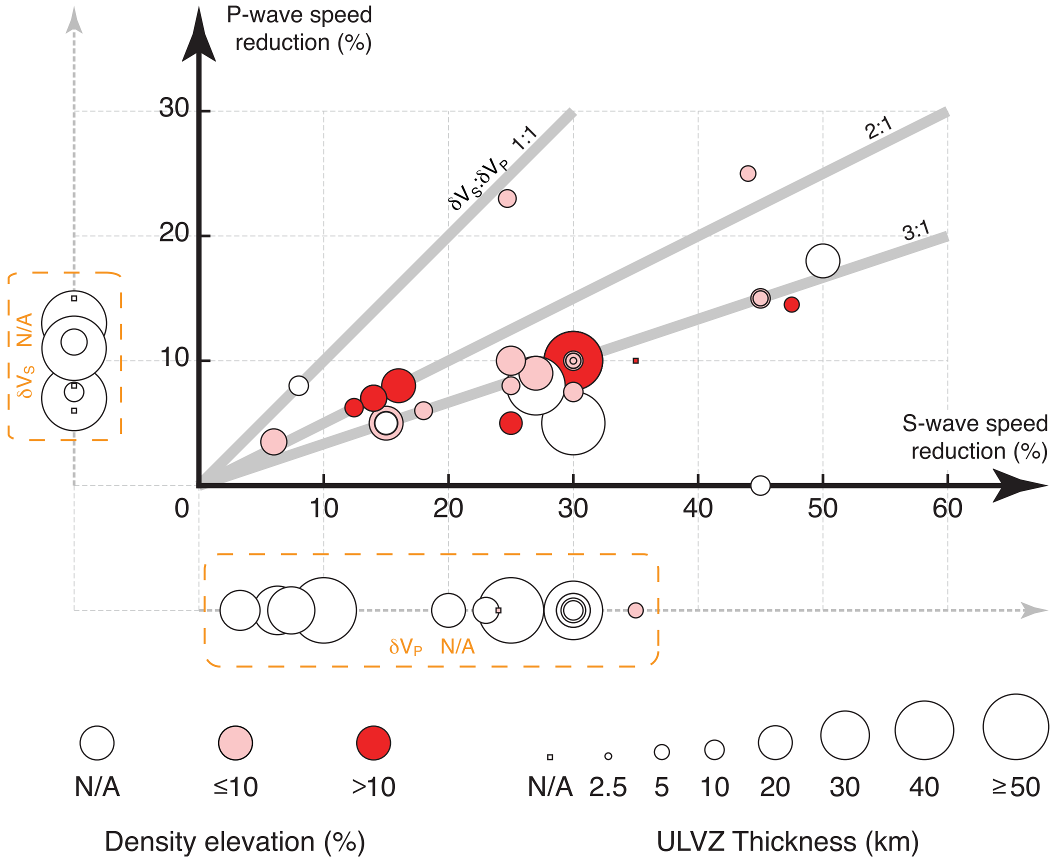

Figure 7. Summary of reported ULVZ properties including *P* wave and *S* wave velocity reduction, density elevation, and ULVZ thickness. Each symbol represents the preferred model from each distinct result in surveyed studies. For studies that only report a *P* wave velocity reduction but no *S* wave information, symbols are plotted along the gray dashed line to the left of the plot domain *y* axis, Similarly, studies only reporting an *S* wave velocity reduction are plotted on the gray dashed line below the plot domain *x* axis. Studies reporting a density elevation are plotted in pink/red symbols, otherwise the symbol color is white. Studies that report a ULVZ thickness are plotted in circles, and sized according to thickness, otherwise they are plotted as small squares. Bold gray lines in the background represent a δV_S:δV_P ratio of 1:1, 2:1, and 3:1.

regions beneath subduction-related downwellings. For example, in S40RTS (Ritsema et al., 2011) at 2,800 km depth, the contour values for the lowest and highest velocity regions amounting to 30% area each are −0.27% and 0.44%, respectively (Figure 8a). Due to ULVZ detection location ambiguities mentioned in section 1.2, only ULVZs identified from reflected wave phases are selected for a calculation of proximity to these velocity regions (Figure 8b). We first decimate ULVZ models and Fresnel zones onto a 0.5° by 0.5° grid at the CMB, then for each ULVZ grid cell, calculate the area and CMB distance to the nearest high and low velocity 30% area δV_S contour. We summarize this information in histograms of fractional accumulated ULVZ area versus distance (Figure 8c). Distances are plotted relative to the low and high δV_S contours. The top plot of Figure 8c is for the low velocity contour (and thus the proxy for LLSVP boundaries). To put the distance scale into perspective, the average distance between the Pacific and African LLSVP boundaries is 4,250 km for model S40RTS (thus ~2,100 km is the average midpoint between the two LLSVPs). The top plot of Figure 8c shows that ULVZs (mapped with reflected seismic waves) tend to be located near LLSVP boundaries, with comparable amounts locating within (~49%) and outside (~51%) of the LLSVPs. On the other hand, the bottom plot of Figure 8c shows the same ULVZs tend to group away from (outside of) the high δV_S (plausibly downwelling) regions. Nonetheless, there is still ~11% of ULVZ areas located within (and near) high δV_S regions.

We explore the stability of this conclusion using two types of tests. In Test I, we randomly populate the CMB with circular shaped ULVZs that add up to the ULVZ area modeled by reflected phases. In reality, due to events and stations having limited spatial distribution, data from reflected phases sample limited CMB

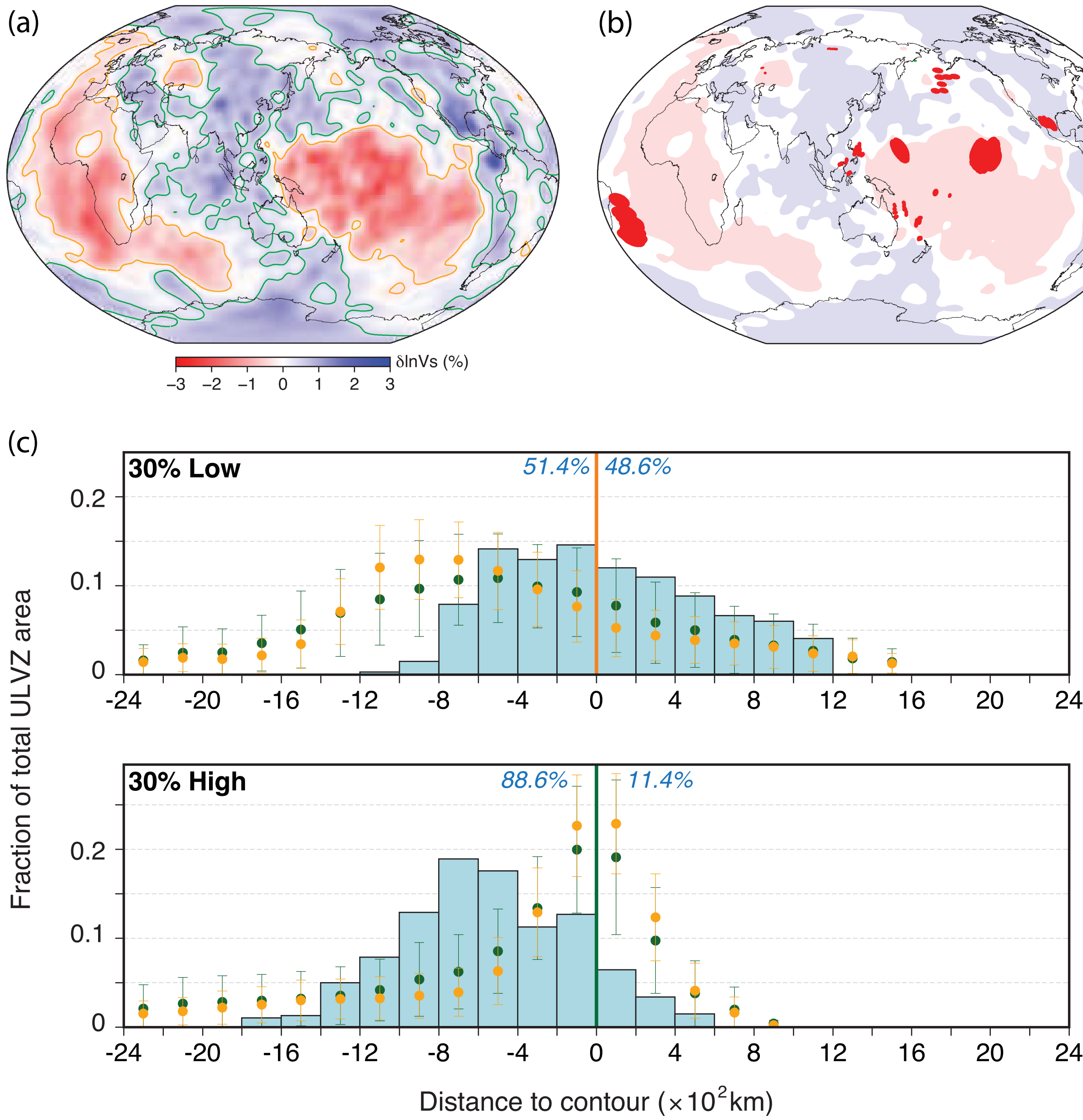

Figure 8. Spatial relation between lowermost mantle structure and ULVZs. Only studies using reflected phases are included (i.e., ScS, ScP, PcP, see text for details). (a) S40RTS (Ritsema et al., 2011) *S* wave anomalies at 2,800 km. Orange lines are *S* wave velocity contours enclosing 30% of the CMB's area containing the lowest wave speeds at 2,800 km depth. Green lines similarly surround 30% of the CMB's area with the highest velocities. The orange contour has value $\delta V_S = -0.27\%$, the green contour corresponds to $\delta V_S = 0.44\%$. (b) The contour enclosed areas in Figure 8a are colored in pink (low velocity) and light blue (high velocity). ULVZs from reflection studies are plotted on top as red regions. (c) Minimum distance of ULVZ areas to the (top plot) low and (bottom plot) high velocity contours. Negative distance means ULVZ areas are located outside of contour enclosed regions, positive means inside. The cumulative ULVZ area outside and inside the contoured regions is shown in the italicized light blue numbers for this model (left is outside contoured regions, right is inside). Orange and dark-green circles represent results from an identical distance measurement calculation, but on random ULVZ distributions: orange corresponds to a random distribution of circular shaped ULVZs; dark-green corresponds to the actual ULVZ data set and distances to random rotations of the tomographic velocity contours (which correspond to Tests I and II in the text). Error bars correspond to the standard deviation of the average of fractional ULVZ area estimated after 1000 random tests (for each of Test I and II).

regions. Therefore, the location of observed ULVZs could be biased by limited path coverage possibilities. To account for this issue, we restrict the locations of randomly populated ULVZs to the CMB regions where CMB sampling is possible (see Figures 9a and 9b, for details). The radius of these circular ULVZs are randomly chosen from 1° up to 6.5°, which spans the range of modeled ULVZ sizes (Figure 9c). Then we calculate the distance-area pattern for this synthetic random ULVZ location scenario in the same way as before. In Test II, 3 random angles are generated, then the contours are rotated around the three perpendicular

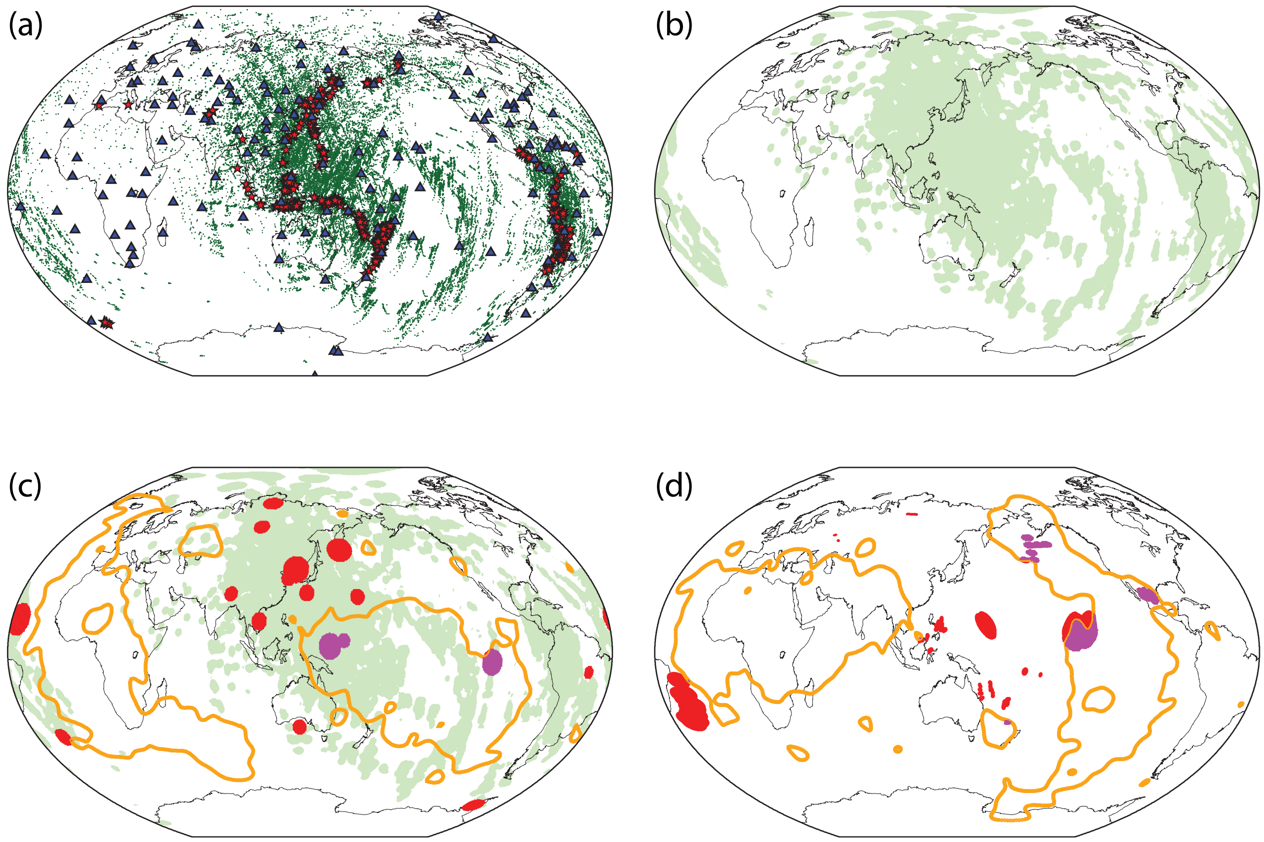

Figure 9. (a) Reflected phases sampling. Red stars: events are from 2005 to 2015 with magnitude greater than 5.7 and source depth greater than 100 km. Blue triangles: 150 stations from the Global Seismic Network (GSN). Green points: calculated theoretical CMB reflection locations from event-station pairs with distance greater than 30° using 1-D model PREM (Dziewonski & Anderson, 1981), for ScS, ScP, and PcP phases. (b) Light green shows the Test I restricted CMB sampling regions, which include locations have at least 20 reflection points within any 2° radius neighborhood. (c) An example from Test I: randomly populated ULVZs within the restricted CMB regions. (d) An example random contour rotation from Test II. In Figures 9c and 9d, the orange lines represent the S40RTS low velocity contours corresponding to LLSVPs with an enclosing area 30% of the CMB. Red regions show ULVZs outside the LLSVPs, and magenta regions are ULVZs inside the LLSVPs. Each of these tests is repeated 1,000 times (see text for more details).

axes with origin at the center of the earth using these three angles (thus, a Eulerian rotation, Figure 9d). After the random rotation, we calculate the distance-area pattern as before. Tests I and II were each repeated 1,000 times before averages and standard deviations were computed for each distance bin. Results are shown as orange (Test I) and dark-green (Test II) filled circles in Figure 8c. The two randomized tests give similar patterns. Both random tests result in the peak ULVZ accumulations shifted to outside LLSVPs compared to observed locations (Figure 8c, top plot). This shift appears robust: the observed ULVZ accumulations lie outside of the standard deviations of both random tests for the distance bins in the range between −1,600 and −800 km. This supports the idea that ULVZs show a likelihood of being spatially correlated with LLSVP boundaries. For the high δV_S regions (Figure 8c, bottom plot), the location of the peaks in the random tests is close to the boundaries, which may relate to the tendency of the high δV_S regions being more linear and less concentrated compared to the particularly concentrated low δV_S regions. We also explore this spatial relationship in the same procedure for another five tomography models: S362ANI + M (Kustowski et al., 2008), HMSL-S06 (Houser et al., 2008), GyPsum (Simmons et al., 2010), SEMUCB-WM1 (French & Romanowicz, 2014), and SP12RTS (Koelemeijer et al., 2016). Results are shown in Figures 10b–10f. The same general patterns are observed for these models. The observations as well as the random test results for model SP12RTS have a broader character to the histogram peaks (Figure 10c, top plot). This is partially due to SP12RTS possessing less short wavelength structure. In contrast, model SEMUCB-WM1 (Figure 10e, top plot) has increased short scale structures outside of the two main LLSVPs—this results in shorter distances to the nearest LLSVP, and hence results in a more concentrated histogram peak.

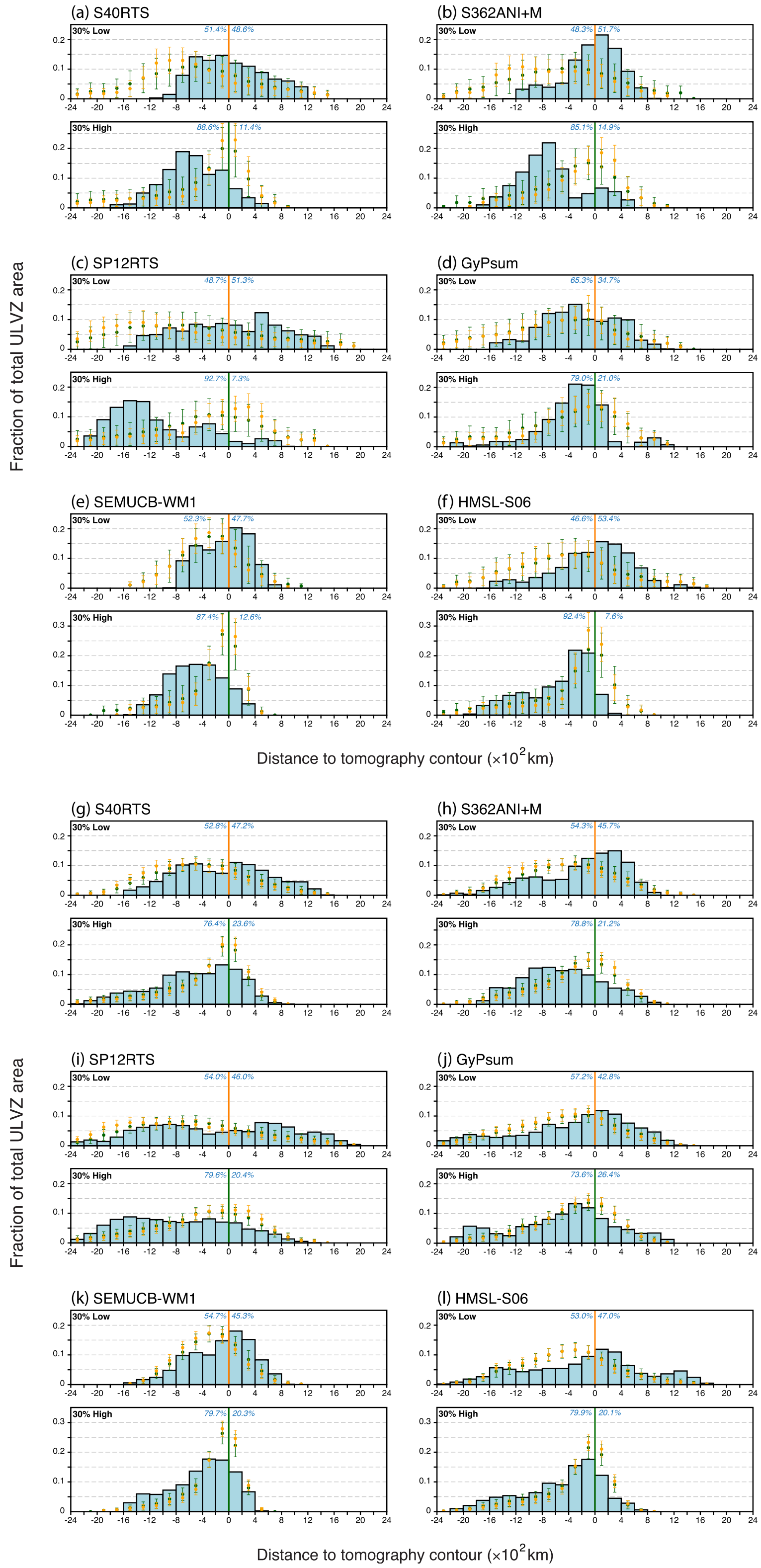

Figure 10. (a–f) Fractional area of observed ULVZs from reflected phases, and (g–l) all phases from all 54 studies with respect to distance to high or low velocity contours in tomographic models (as in Figure 8c), for tomography models (a) and (g) S40RTS (Ritsema et al., 2011), (b) and (h) S362ANI + M (Kustowski et al., 2008), (c) and (i) SP12RTS (Koelemeijer et al., 2016), (d) and (j) GyPsum (Simmons et al., 2010), (e) and (k) SEMUCB-WM1 (French & Romanowicz, 2014), and (f) and (l) HMSL-S06 (Houser et al., 2008).

We also explore the pattern of ULVZ proximity to high and low velocity zone boundaries for ULVZs of all 54 studies (Figure 6a), which are presented in Figures 10g–10l for the six tomography models shown in Figures 10a–10f. Similar to Test I, we computed random populated ULVZ statistics but without sampling-region restriction, mainly because the ULVZ location ambiguity for nonreflection phases used in ULVZ studies. Since the ULVZs are more widely distributed than those of solely the reflected wave studies, the histograms are somewhat more spread out than those of Figures 10a–10f. More rigorous tests are possible, however, they would be warranted with a more geographically comprehensive ULVZ catalog.

4.2. Hot Spots and ULVZs

Hot spots have long been considered linked to whole mantle plumes (Morgan, 1971). While not every hot spot may signify a surface to CMB connection (Courtillot et al., 2003), a connection to ULVZs has been made in several studies (e.g., Cottaar & Romanowicz, 2012; Helmberger et al., 1998; Wen, 2000; Williams et al., 1998; Yuan & Romanowicz, 2017). Also, a link between hot spots and LLSVP margins (Thorne et al., 2004; Torsvik et al., 2014), combined with the ULVZs appearing to group near LLSVP margins (Figure 8a), motivates a plot of minimum distance between ULVZs and hot spots (similar to that in Figure 8c). We use a compilation of 61 hot spots locations from Morgan and Morgan (2007). Of those hot spots, seven possible deep-sourced ones are identified in Courtillot et al. (2003). For the surface location of each hot spot, we find the distance along the CMB to the nearest ULVZ. Figure 11 displays the results (similar to that done in Figure 8). We conduct random ULVZ location and random hot spot rotation tests (similar to that with LLSVPs in Figure 8c). Figures 11a and 11b only consider ULVZs reported from reflected wave studies. There is no clear association for ULVZs to be associated with hot spot locations, however, the CMB sampling coverage is low for reflected wave analyses. The presumed deep plume hot spots (thick crosses in Figure 11b) are similarly

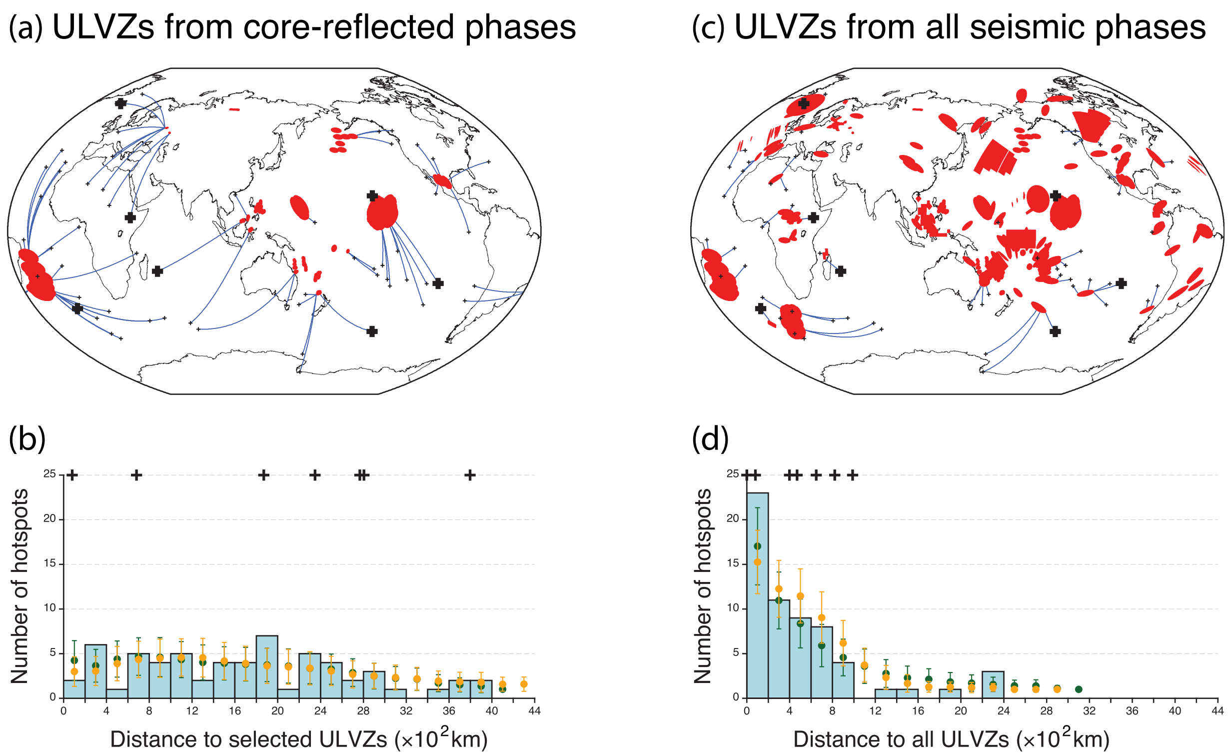

Figure 11. Spatial relation between surface hot spots and ULVZs. (a) and (b) Are for ULVZ zones mapped using core-reflected phases (ScS, ScP, and PcP). In Figure 11a, ULVZs are shown as red regions and hot spot locations are black crosses; the larger and bold crosses are the seven hot spots noted for having possible deep plume sources (*Courtillot et al*., 2003). The blue lines depict the shortest path between each hot spot and the nearest ULVZ. In Figure 11b, the number of hot spots for different distance to ULVZ bins are shown (blue histogram bars), along with the same measurements for the random ULVZ distributions of Test I (orange-filled circles, for sampling-region-restricted randomly located circular shaped ULVZs) and Test II (dark green-filled circles, for random rotations of the hot spots). The distance for the seven deep-sourced hot spots are denoted at the top as black crosses. Plots (c) and (d) are identical to (a) and (b), except computations are done using ULVZs imaged with any seismic phase, also, with the geographic domain of ULVZs in Test I being global. In this case, hot spots show a relationship to ULVZ locations, but statistical significance is not established.

uncorrelated in distance. The random tests mimic the observed trend: ULVZs do not show distance preference to hot spot locations (orange-filled circles); the random rotations of the hot spot reference frame (green-filled circles), similarly does not demonstrate any trend with distance.

The story changes when all the ULVZ locations (from Figure 6a) are considered. Figures 11c and 11d show the result, which indicates that significantly more hot spots are close to ULVZ locations than far away from them. Some recent ULVZ studies beneath deep plume hot spot volcanoes have found the largest volume ULVZs to date, namely, Hawaii (Cottaar & Romanowicz, 2012), Samoa (Thorne et al., 2013) and Iceland (Yuan & Romanowicz, 2017). Here we find that the deep plume hot spots are no more than 1,000 km away from any mapped ULVZ, and that more than 90% of the 61 hot spots (from Morgan & Morgan, 2007) are within 1,000 km of a ULVZ, and 38% of them are within 200 km away. Our random tests, however, suggest that these correlations do not hold statistical significance. Both Test I (for the globally randomized ULVZ locations) and Test II (random rotation of hot spots) produce a similar pattern to that which is observed. It could very well be that hot spots are well correlated to ULVZs, but that some of the ULVZs placed on source or receiver sides of path (e.g., from some SP_dKS analyses) are erroneous, thus yielding an artificially higher small-distance hot spot count in our observation. Also, many ULVZs, especially if compositionally distinct, may be initially far from plumes but advecting toward plume zones (Yuan & Romanowicz, 2017) or thermochemical piles (Garnero et al., 2016; Li et al., 2017).

5. Discussion

5.1. Current CMB Coverage

Our Fresnel zone representations of ULVZs combined with defined ULVZ zones from published models cover roughly 17.1% of the CMB, by area. Positive ULVZ detection amounts to over 10.3% of the total CMB, and 6.5% of the CMB's area lacks ULVZ evidence. The complex data regions account for 3.8% of the CMB's area (we note that some regions have multiple ULVZ classifications, i.e., presence, absence, and complex). Other CMB areas may have been sampled, but normal and complex data regions may have been left unreported.

A typical ULVZ detection threshold for reflected waves phase is around 5 km in thickness (though some array methodologies using high frequency data can detect thinner ULVZs, e.g., Rost et al., 2010a). The minimum thickness detection threshold will be larger for longer period waves, such as diffracted waves. It will also be larger if the ULVZ properties are less extreme, owing to the classic trade-off between ULVZ thickness and velocity reduction (e.g., Garnero & Helmberger, 1998; Rost et al., 2006). Therefore, it is possible that ULVZs may exist in sampled areas that have been designated as lacking ULVZs, if the structure is thin and/or the properties are not particularly anomalous. This raises the possibility of a global ULVZ layer that is too thin to detect, but only appears where the mantle is hot, upwelling, or convection has generated accumulations of distinct ULVZ material (Figure 1d).

5.2. Conflicting Results

We observed regions where ULVZ detection overlapped with ULVZ nondetection (Figure 6e). While our Fresnel zones are reasonable approximations to the CMB area that contributes to waveform distortions caused by ULVZs, it is always possible to have sub-Fresnel zone variations in structure. Such a dual classification is not particularly common in the studies presented here: only 1.7% of the CMB area has models advocating both ULVZ presence and absence (i.e., about 10% of the surveyed CMB area). Consideration of finite frequency effects for the sensitivity of different probes to structure at the CMB will be an important next step in future studies.

6. Conclusion

We digitized the locations and models of ULVZs in 54 past studies. Locations of ULVZ presence and absence were digitized, as well as regions which authors depicted as unsure or uncertain, due to data complexities. This database contains five types of information: (1) the digitized bouncing locations for the core-reflected phases PcP, ScP, and ScS; (2) the digitized ray path segments for diffraction at the CMB associated with the phases SP_dKS, $PKKP_{ab\_diff}$, P_{diff}, and S_{diff}; (3) the digitized high likelihood ULVZ zones for PKP scatterers; (4) the digitized area associated with ULVZ model regions presented in some studies; and (5) estimation of

Fresnel zones (digitized) for the information in (1) and (2). This database can be freely accessed (Yu & Garnero, 2017). ULVZs appear to be mostly correlated with low velocity regions in the lowermost mantle, and in particular, are commonly found near LLSVP margins. While not statistically significant with the distribution of ULVZs studied, there is a preference for ULVZs to be found beneath or near many hot spots.

Acknowledgments
We are grateful to a number of ULVZ researchers that freely shared ULVZ model and location information from their past studies. Valuable discussions with Mingming Li and Allen McNamara inspired some of the analyses in this project. The manuscript greatly benefitted from careful reviews by Sanne Cottaar and Michael Thorne. We also are grateful for the GraphClick freeware program, which was downloaded from http://www.arizona-software.ch/graphclick/ as well as the Generic Mapping Tools freeware package (Wessel et al., 2013), downloaded from http://gmt.soest.hawaii.edu/projects/gmt. The ULVZ database (Yu & Garnero, 2017) will be updated as new ULVZ studies come out. We encourage authors of new ULVZ studies contact us. We will also actively and regularly search for new ULVZ studies. The DOI in the Reference list links to the most current version of the database. This work was supported by NSF grants EAR-1648817 and EAR-1401270.

References

Andrault, D., Pesce, G., Bouhifd, M. A., Bolfan-Casanova, N., Henot, J. M., & Mezouar, M. (2014). Melting of subducted basalt at the core-mantle boundary. *Science*, *344*(6186), 892–895. https://doi.org/10.1126/science.1250466

Avants, M., Lay, T., & Garnero, E. J. (2006). A new probe of ULVZ S-wave velocity structure: Array stacking of ScS waveforms. *Geophysical Research Letters*, *33*, L07314. https://doi.org/10.1029/2005GL024989

Berryman, J. G. (2000). Seismic velocity decrement ratios for regions of partial melt in the lower mantle. *Geophysical Research Letters*, *27*(3), 421–424. https://doi.org/10.1029/1999GL008402

Brown, S. P., Thorne, M. S., Miyagi, L., & Rost, S. (2015). A compositional origin to ultralow-velocity zones. *Geophysical Research Letters*, *42*, 1039–1045. https://doi.org/10.1002/2014GL062097

Buffett, B. A., Garnero, E. J., & Jeanloz, R. (2000). Sediments at the Top of Earth's Core. *Science*, *290*(5495), 1338–1342. https://doi.org/10.1126/science.290.5495.1338

Castle, J. C., & Van Der Hilst, R. D. (2000). The core–mantle boundary under the Gulf of Alaska: No ULVZ for shear waves. *Earth and Planetary Science Letters*, *176*(3–4), 311–321. https://doi.org/10.1016/S0012-821X(00)00027-3

Cottaar, S., & Romanowicz, B. (2012). An unusually large ULVZ at the base of the mantle near Hawaii. *Earth and Planetary Science Letters*, *355–356*, 213–222. https://doi.org/10.1016/j.epsl.2012.09.005

Courtier, A. M., Bagley, B., & Revenaugh, J. (2007). Whole mantle discontinuity structure beneath Hawaii. *Geophysical Research Letters*, *34*, L17304. https://doi.org/10.1029/2007GL031006

Courtillot, V., Davaille, A., Besse, J., & Stock, J. (2003). Three distinct types of hotspots in the Earth's mantle. *Earth and Planetary Science Letters*, *205*(3–4), 295–308. https://doi.org/10.1016/S0012-821X(02)01048-8

Dobson, D. P., & Brodholt, J. P. (2005). Subducted banded iron formations as a source of ultralow-velocity zones at the core-mantle boundary. *Nature*, *434*(7031), 371–374. https://doi.org/10.1038/nature03430

Dziewonski, A. M., & Anderson, D. L. (1981). Preliminary reference Earth model. *Physics of the Earth and Planetary Interiors*, *25*(4), 297–356. https://doi.org/10.1016/0031-9201(81)90046-7

French, S. W., & Romanowicz, B. A. (2014). Whole-mantle radially anisotropic shear velocity structure from spectral-element waveform tomography. *Geophysical Journal International*, *199*(3), 1303–1327. https://doi.org/10.1093/gji/ggu334

Garnero, E. J., & Helmberger, D. V. (1998). Further structural constraints and uncertainties of a thin laterally varying ultralow-velocity layer at the base of the mantle. *Journal of Geophysical Research*, *103*(B6), 12495–12509.

Garnero, E. J., McNamara, A. K., & Shim, S.-H. (2016). Continent-sized anomalous zones with low seismic velocity at the base of Earth's mantle. *Nature Geoscience*, *9*(7), 481–489. https://doi.org/10.1038/ngeo2733

Garnero, E. J., & Vidale, J. E. (1999). ScP: A probe of ultralow velocity zones at the base of the mantle. *Geophysical Research Letters*, *26*(3), 377–380. https://doi.org/10.1029/1998GL900319

Gassner, A., Thomas, C., Krüger, F., & Weber, M. (2015). Probing the core-mantle boundary beneath Europe and Western Eurasia: A detailed study using PcP. *Physics of the Earth and Planetary Interiors*, *246*, 9–24. https://doi.org/10.1016/j.pepi.2015.06.007

Havens, E., & Revenaugh, J. (2001). A broadband seismic study of the lowermost mantle beneath Mexico: Constraints on ultralow velocity zone elasticity and density. *Journal of Geophysical Research: Solid Earth*, *106*(B12), 30809–30820. https://doi.org/10.1029/2000JB000072

He, Y., & Wen, L. (2009). Structural features and shear-velocity structure of the "Pacific Anomaly. *Journal of Geophysical Research: Solid Earth*, *114*, L07314. https://doi.org/10.1029/2008JB005814

Helmberger, D., Ni, S., Wen, L., & Ritsema, J. (2000). Seismic evidence for ultralow-velocity zones beneath Africa and eastern Atlantic. *Journal of Geophysical Research: Solid Earth*, *105*(B10), 23865–23878. https://doi.org/10.1029/2000JB900143

Helmberger, D. V., Wen, L., & Ding, X. (1998). Seismic evidence that the source of the Iceland hotspot lies at the core-mantle boundary. *Nature*, *396*(6708), 251–255. https://doi.org/10.1038/24357

Hernlund, J. W., & McNamara, A. K. (2015). The core-mantle boundary region. In G. Schubert & D. Bercovici (Eds.), *Treatise on geophysics* (pp. 461–519). Amsterdam, the Netherlands: Elsevier.

Hernlund, J. W., & Tackley, P. J. (2007). Some dynamical consequences of partial melting in Earth's deep mantle. *Physics of the Earth and Planetary Interiors*, *162*(1–2), 149–163. https://doi.org/10.1016/j.pepi.2007.04.005

Houser, C., Masters, G., Shearer, P., & Laske, G. (2008). Shear and compressional velocity models of the mantle from cluster analysis of long-period waveforms. *Geophysical Journal International*, *174*(1), 195–212. https://doi.org/10.1111/j.1365-246X.2008.03763.x

Hu, Q., Kim, D. Y., Yang, W., Yang, L., Meng, Y., Zhang, L., et al. (2016). FeO_2 and FeOOH under deep lower-mantle conditions and Earth's oxygen-hydrogen cycles. *Nature*, *534*(7606), 241–244. https://doi.org/10.1038/nature18018

Hutko, A. R., Lay, T., & Revenaugh, J. (2009). Localized double-array stacking analysis of PcP: D″ and ULVZ structure beneath the Cocos plate, Mexico, central Pacific, and north Pacific. *Physics of the Earth and Planetary Interiors*, *173*(1–2), 60–74. https://doi.org/10.1016/j.pepi.2008.11.003

Idehara, K. (2011). Structural heterogeneity of an ultra-low-velocity zone beneath the Philippine Islands: Implications for core-mantle chemical interactions induced by massive partial melting at the bottom of the mantle. *Physics of the Earth and Planetary Interiors*, *184*(1–2), 80–90. https://doi.org/10.1016/j.pepi.2010.10.014

Idehara, K., Yamada, A., & Zhao, D. (2007). Seismological constraints on the ultralow velocity zones in the lowermost mantle from core-reflected waves. *Physics of the Earth and Planetary Interiors*, *165*(1–2), 25–46. https://doi.org/10.1016/j.pepi.2007.07.005

Jensen, K. J., Thorne, M. S., & Rost, S. (2013). SPdKS analysis of ultralow-velocity zones beneath the western Pacific. *Geophysical Research Letters*, *40*, 4574–4578. https://doi.org/10.1002/grl.50877

Koelemeijer, P., Ritsema, J., Deuss, A., & Van Heijst, H. J. (2016). SP12RTS: A degree-12 model of shear- and compressional-wave velocity for Earth's mantle. *Geophysical Journal International*, *204*(2), 1024–1039. https://doi.org/10.1093/gji/ggv481

Kohler, M. D., Vidale, J. E., & Davis, P. M. (1997). Complex scattering within D″ observed on the very dense Los Angeles Region Seismic Experiment Passive Array. *Geophysical Research Letters*, *24*(15), 1855–1858. https://doi.org/10.1029/97GL01823

Koper, K. D., & Pyle, M. L. (2004). Observations of PKiKP/PcP amplitude ratios and implications for Earth structure at the boundaries of the liquid core. *Journal of Geophysical Research: Solid Earth*, *109*, B03301. https://doi.org/10.1029/2003JB002750

Kustowski, B., Ekström, G., & Dziewoński, A. M. (2008). Anisotropic shear-wave velocity structure of the Earth's mantle: A global model. *Journal of Geophysical Research: Solid Earth*, *113*, B06306. https://doi.org/10.1029/2007JB005169

Li, M., McNamara, A. K., Garnero, E. J., & Yu, S. (2017). Compositionally-distinct ultra-low velocity zones on Earth's core-mantle boundary. *Nature Communications*, *8*(1), 177. https://doi.org/10.1038/s41467-017-00219-x

Liu, J., Li, J., Hrubiak, R., & Smith, J. S. (2016). Origins of ultralow velocity zones through slab-derived metallic melt. *Proceedings of the National Academy of Sciences of the United States of America*, *113*(20), 5547–5551. https://doi.org/10.1073/pnas.1519540113

Luo, S. N., Ni, S., & Helmberger, D. V. (2001). Evidence for a sharp lateral variation of velocity at the core-mantle boundary from multipathed PKPab. *Earth and Planetary Science Letters*, *189*(3–4), 155–164. https://doi.org/10.1016/S0012-821X(01)00364-8

Mao, W. L., Mao, H.-K., Sturhahn, W., Zhao, J., Prakapenka, V. B., Meng, Y., et al. (2006). Iron-rich post-perovskite and the origin of ultralow-velocity zones. *Science*, *312*(5773), 564–565. https://doi.org/10.1126/science.1123442

McNamara, A. K., Garnero, E. J., & Rost, S. (2010). Tracking deep mantle reservoirs with ultra-low velocity zones. *Earth and Planetary Science Letters*, *299*(1–2), 1–9. https://doi.org/10.1016/j.epsl.2010.07.042

McNamara, A. K., & Zhong, S. (2005). Thermochemical structures beneath Africa and the Pacific Ocean. *Nature*, *437*(7062), 1136–1139. https://doi.org/10.1038/nature04066

Morgan, W. J. (1971). Convection plumes in the lower mantle. *Nature*, *230*(5288), 42–43. https://doi.org/10.1038/230042a0

Morgan, W. J., & Morgan, J. P. (2007). Plate velocities in the hotspot reference frame. *Geological Society of America Special Papers*, *430*, 65–78, https://doi.org/10.1130/2007.2430(04)

Mori, J., & Helmberger, D. V. (1995). Localized boundary layer below the mid-Pacific velocity anomaly identified from a PcP precursor. *Journal of Geophysical Research*, *100*(B10), 20359–20365. https://doi.org/10.1029/95JB02243

Ni, S., & Helmberger, D. V. (2001a). Horizontal transition from fast to slow structures at the core-mantle boundary; South Atlantic. *Earth and Planetary Science Letters*, *187*(3–4), 301–310. https://doi.org/10.1016/S0012-821X(01)00273-4

Ni, S., & Helmberger, D. V. (2001b). Probing an ultra-low velocity zone at the core mantle boundary with P and S waves. *Geophysical Research Letters*, *28*(12), 2345–2348. https://doi.org/10.1029/2000GL012766

Niu, F., & Wen, L. (2001). Strong seismic scatterers near the core-mantle boundary west of Mexico. *Geophysical Research Letters*, *28*(18), 3557–3560. https://doi.org/10.1029/2001GL013270

Nomura, R., Hirose, K., Uesugi, K., Ohishi, Y., Tsuchiyama, A., Miyake, A., et al. (2014). Low core-mantle boundary temperature inferred from the solidus of pyrolite. *Science*, *343*(6170), 522–525. https://doi.org/10.1126/science.1248186

Pachhai, S., Dettmer, J., & Tkalčić, H. (2015). Ultra-low velocity zones beneath the Philippine and Tasman Seas revealed by a trans-dimensional Bayesian waveform inversion. *Geophysical Journal International*, *203*(2), 1302–1318. https://doi.org/10.1093/gji/ggv368

Persh, S. E., Vidale, J. E., & Earle, P. S. (2001). Absence of short-period ULVZ precursors to PcP and ScP from two regions of the CMB. *Geophysical Research Letters*, *28*(2), 387–390. https://doi.org/10.1029/2000GL011607

Reasoner, C., & Revenaugh, J. (2000). ScP constraints on ultralow-velocity zone density and gradient thickness beneath the Pacific. *Journal of Geophysical Research: Solid Earth*, *105*(B12), 28173–28182. https://doi.org/10.1029/2000JB900331

Revenaugh, J., & Meyer, R. (1997). Seismic evidence of partial melt within a possibly ubiquitous low-velocity layer at the base of the mantle. *Science*, *277*(5326), 670–673. https://doi.org/10.1126/science.277.5326.670

Ritsema, J., Deuss, A., Van Heijst, H. J., & Woodhouse, J. H. (2011). S40RTS: A degree-40 shear-velocity model for the mantle from new Rayleigh wave dispersion, teleseismic traveltime and normal-mode splitting function measurements. *Geophysical Journal International*, *184*(3), 1223–1236.

Rondenay, S., & Fischer, K. M. (2003). Constraints on localized core-mantle boundary structure from multichannel, broadband SKS coda analysis. *Journal of Geophysical Research: Solid Earth*, *108*(B11), 2537. https://doi.org/10.1029/2003JB002518

Ross, A. R., Thybo, H., & Solidilov, L. N. (2004). Reflection seismic profiles of the core-mantle boundary. *Journal of Geophysical Research: Solid Earth*, *109*, B08303. https://doi.org/10.1029/2003JB002515

Rost, S., & Thomas, C. (2010). High resolution CMB imaging from migration of short-period core reflected phases. *Physics of the Earth and Planetary Interiors*, *183*(1–2), 143–150. https://doi.org/10.1016/j.pepi.2010.04.005

Rost, S., & Garnero, E. J. (2006). Detection of an ultralow velocity zone at the core-mantle boundary using diffracted PKKPab waves. *Journal of Geophysical Research: Solid Earth*, *111*, B07309. https://doi.org/10.1029/2005JB003850

Rost, S., & Revenaugh, J. (2001). Seismic detection of rigid zones at the top of the core. *Science*, *294*(5548), 1911–1914. https://doi.org/10.1126/science.1065617

Rost, S., & Revenaugh, J. (2003). Small-scale ultralow-velocity zone structure imaged by ScP. *Journal of Geophysical Research: Solid Earth*, *108*(B1), 2056. https://doi.org/10.1029/2001JB001627

Rost, S., Garnero, E. J., & Stefan, W. (2010a). Thin and intermittent ultralow-velocity zones. *Journal of Geophysical Research: Solid Earth*, *115*, B06312. https://doi.org/10.1029/2009JB006981

Rost, S., Garnero, E. J., Thorne, M. S., & Hutko, A. R. (2010b). On the absence of an ultralow-velocity zone in the North Pacific. *Journal of Geophysical Research: Solid Earth*, *115*, L14612. https://doi.org/10.1029/2009JB006420

Rost, S., Garnero, E. J., & Williams, Q. (2006). Fine-scale ultralow-velocity zone structure from high-frequency seismic array data. *Journal of Geophysical Research: Solid Earth*, *111*, B09310. https://doi.org/10.1029/2005JB004088

Rost, S., Garnero, E. J., Williams, Q., & Manga, M. (2005). Seismological constraints on a possible plume root at the core-mantle boundary. *Nature*, *435*(7042), 666–669. https://doi.org/10.1038/nature03620

Silver, P. G., & Bina, C. (1993). An anomaly in the amplitude ratio of SKKS/SKS in the range 100–108° from portable teleseismic data. *Geophysical Research Letters*, *20*(12), 1135–1138. https://doi.org/10.1029/92GL02464

Simmons, N. A., Forte, A. M., Boschi, L., & Grand, S. P. (2010). GyPSuM: A joint tomographic model of mantle density and seismic wave speeds. *Journal of Geophysical Research: Solid Earth*, *115*, B12310. https://doi.org/10.1029/2010JB007631

Simmons, N. A., & Grand, S. P. (2002). Partial melting in the deepest mantle. *Geophysical Research Letters*, *29*(11), 1552. https://doi.org/10.1029/2001GL013716

Sun, D., Helmberger, D., Ni, S., & Bower, D. (2009). Direct measures of lateral velocity variation in the deep Earth. *Journal of Geophysical Research: Solid Earth*, *114*, B05303. https://doi.org/10.1029/2008JB005873

Thomas, C., Kendall, J.-M., & Helffrich, G. (2009). Probing two low-velocity regions with PKPb-caustic amplitudes and scattering. *Geophysical Journal International*, *178*(1), 503–512. https://doi.org/10.1111/j.1365-246X.2009.04189.x

Thomas, C., Weber, M., Wicks, C. W., & Scherbaum, F. (1999). Small scatterers in the lower mantle observed at German broadband arrays. *Journal of Geophysical Research: Solid Earth*, *104*(B7), 15073–15088. https://doi.org/10.1029/1999JB900128

Thorne, M. S., & Garnero, E. J. (2004). Inferences on ultralow-velocity zone structure from a global analysis of SPdKS waves. *Journal of Geophysical Research: Solid Earth*, *109*, B08301. https://doi.org/10.1029/2004JB003010

Thorne, M. S., Garnero, E. J., & Grand, S. P. (2004). Geographic correlation between hot spots and deep mantle lateral shear-wave velocity gradients. *Physics of the Earth and Planetary Interiors*, *146*(1–2), 47–63. https://doi.org/10.1016/j.pepi.2003.09.026

Thorne, M. S., Garnero, E. J., Jahnke, G., Igel, H., & McNamara, A. K. (2013). Mega ultra low velocity zone and mantle flow. *Earth and Planetary Science Letters*, *364*, 59–67. https://doi.org/10.1016/j.epsl.2012.12.034

To, A., Fukao, Y., & Tsuboi, S. (2011). Evidence for a thick and localized ultra low shear velocity zone at the base of the mantle beneath the central Pacific. *Physics of the Earth and Planetary Interiors*, *184*(3–4), 119–133. https://doi.org/10.1016/j.pepi.2010.10.015

Torsvik, T. H., van der Voo, R., Doubrovine, P. V., Burke, K., Steinberger, B., Ashwal, L. D., et al. (2014). Deep mantle structure as a reference frame for movements in and on the Earth. *Proceedings of the National Academy of Sciences of United States of America*, *111*(24), 8735–8740. https://doi.org/10.1073/pnas.1318135111

Tsuchiya, T., & Tsuchiya, J. (2006). Effect of impurity on the elasticity of perovskite and postperovskite: Velocity contrast across the postperovskite transition in (Mg,Fe,Al)(Si,Al)O 3. *Geophysical Research Letters*, *33*, L12S04. https://doi.org/10.1029/2006GL025706

Vanacore, E. A., Rost, S., & Thorne, M. S. (2016). Ultralow-velocity zone geometries resolved by multidimensional waveform modelling. *Geophysical Journal International*, *206*(1), 659–674. https://doi.org/10.1093/gji/ggw114

Vidale, J. E., & Benz, H. M. (1992). A sharp and flat section of the core-mantle boundary. *Nature*, *359*(6396), 627–629. https://doi.org/10.1038/359627a0

Vidale, J. E., & Hedlin, M. A. H. (1998). Evidence for partial melt at the core-mantle boundary north of Tonga from the strong scattering of seismic waves. *Nature*, *391*(6668), 682–685. https://doi.org/10.1038/35601

Wen, L. (2000). Intense seismic scattering near the Earth's core-mantle boundary beneath the Comoros hotspot. *Geophysical Research Letters*, *27*(22), 3627–3630. https://doi.org/10.1029/2000GL011831

Wen, L., & Helmberger, D. V. (1998a). Ultra-low velocity zones near the core-mantle boundary from broadband PKP precursors. *Science*, *279*(5357), 1701–1703. https://doi.org/10.1126/science.279.5357.1701

Wen, L., & Helmberger, D. V. (1998b). A two-dimensional P-SV hybrid method and its application to modeling localized structures near the core-mantle boundary. *Journal of Geophysical Research: Solid Earth*, *103*(B8), 17901–17918. https://doi.org/10.1029/98JB01276

Wessel, P., Smith, W. H. F., Scharroo, R., Luis, J., & Wobbe, F. (2013). Generic mapping tools: Improved version released. *Eos, Transactions American Geophysical Union*, *94*(45), 409–410. https://doi.org/10.1002/2013EO450001

Wicks, J. K., Jackson, J. M., Sturhahn, W., & Zhang, D. (2017). Sound velocity and density of magnesiowüstites: Implications for ultralow-velocity zone topography. *Geophysical Research Letters*, *44*, 2148–2158. https://doi.org/10.1002/2016GL071225

Williams, Q., & Garnero, E. J. (1996). Seismic evidence for partial melt at the base of Earth's mantle. *Science*, *273*(5281), 1528–1530. doi: 10.1126/science.273.5281.1528.

Williams, Q., Revenaugh, J., & Garnero, E. J. (1998). A correlation between ultra-low basal velocities in the mantle and hot spots. *Science*, *281*(5376), 546–549. https://doi.org/10.1126/science.281.5376.546

Xu, Y., & Koper, K. D. (2009). Detection of a ULVZ at the base of the mantle beneath the northwest Pacific. *Geophysical Research Letters*, *36*, L14612. https://doi.org/10.1029/2009GL039387

Yao, J., & Wen, L. (2014). Seismic structure and ultra-low velocity zones at the base of the Earth's mantle beneath Southeast Asia. *Physics of the Earth and Planetary Interiors*, *233*, 103–111. https://doi.org/10.1016/j.pepi.2014.05.009

Yu, S., & Garnero, E. J. (2017). ULVZ Distribution Database from 54 studies [Data set]. Zenodo. http://doi.org/10.5281/zenodo.1000998

Yuan, K., & Romanowicz, B. (2017). Seismic evidence for partial melting at the root of major hot spot plumes. *Science*, *357*(6349), 393–397. https://doi.org/10.1126/science.aan0760

Zhang, Y., Ritsema, J., & Thorne, M. S. (2009). Modeling the ratios of SKKS and SKS amplitudes with ultra-low velocity zones at the core-mantle boundary, *Geophysical Research Letters*, *36*, L19303. https://doi.org/10.1029/2009GL040030

Zhao, C., Garnero, E. J., Li, M., McNamara, A., & Yu, S. (2017). Intermittent and lateral varying ULVZ structure at the northeastern margin of the Pacific LLSVP. *Journal of Geophysical Research: Solid Earth*, *122*, 1198–1220. https://doi.org/10.1002/2016JB013449

Zou, Z., Leyton, F., & Koper, K. D. (2007). Partial melt in the lowermost mantle near the base of a plume. *Geophysical Journal International*, *168*(2), 809–817. https://doi.org/10.1111/j.1365-246X.2006.03266.x